AIAA Guidance, Navigation and Control Conference and Exhibit
20 - 23 August 2007, Hilton Head, South Carolina

AIAA 2007-6770

# Autolanding Controller for a Fixed Wing Unmanned Air Vehicle

Paulo Rosa*, Carlos Silvestre†, David Cabecinhas‡, Rita Cunha§

*Instituto Superior Técnico, Institute for Systems and Robotics, 1049-001 Lisbon, Portugal*

**This paper addresses the autolanding guidance and control problem for unmanned autonomous vehicles (UAV) based on the information provided by the onboard Navigation System. The proposed solution relies on a path-following and velocity profile tracking controller synthesized using an accurate aircraft dynamic model, referred to as *SymAirDyn*, which was designed with the objective of exploiting the whole aircraft's flight envelope. A suitable polytopic Linear Parameter Varying (LPV) representation with piecewise affine dependence on the parameters is adopted to accurately model the desired aircraft dynamics over a set of predefined operating regions. The synthesis problem is stated as a continuous-time $H_2$ control problem for LPV systems and solved using Linear Matrix Inequalities (LMIs). During the controller design stage, the aircraft landing maneuver is decomposed in the two standard phases: the glideslope and the flare. For each phase, the required control objectives are identified and specific controllers are designed. The controller implementation is tackled within the framework of gain-scheduling control theory using the D-methodology. The performance and effectiveness of the resulting nonlinear gain scheduling controller is illustrated in simulation, using the nonlinear model *SymAirDyn* under different types of disturbances, namely Dryden spectrum generated wind during the glideslope and wind gusts near touchdown.**

## I. Introduction

Over the last decade, the advent of new sensor technology and the successes of already deployed platforms have bolstered a worldwide interest on developing and expanding the capabilities of Unmanned Air Vehicles (UAVs). A remarkably wide spectrum of UAV configurations is currently in use or under development, ranging from fixed and rotary wing, going from micro to jet-sized. Fixed wing UAVs are already being used in commercial applications such as rice fields spraying and fish banks search in Japan. Companies like Scandicraft, Schiebel and Yamaha have industrial helicopters available for filming operations in risk situations. Other applications that are currently being brought forward include maintenance and security inspection of power lines, and oil and gas pipelines; forest fire surveillance; environmental observation and monitoring of natural disaster areas; among others.

The advent of new empowering stand-alone sensors, such as the Laser Range Finder and GPS has encouraged the adoption of onboard positioning and enhanced the navigation systems. These systems are currently recognized as instrumental in bringing about all the capabilities of an UAV to perform high precision tasks in challenging and uncertain operation scenarios. Several different methods have been proposed and flight tested,[1–3] confirming the expected robustness and performance that can be achieved in the execution of specific maneuvers, such as landing or steering the vehicle to a desired target.

Nowadays airports are equipped with runway approaching systems that provide lateral and vertical guidance to aircrafts during the glideslope and final landing maneuver. A common mechanism is the so-called Instrument Landing System (ILS)[4] that is composed of several radio beacons placed on the runway, allowing for vertical and lateral accurate guidance of the aircraft during the landing phase. Once the approaching

*PhD Student, Department of Electrical Engineering and Computer Science (DEEC), Av. Rovisco Pais 1; prosa@isr.ist.utl.pt.

†Assistant Professor, DEEC, Av. Rovisco Pais 1; cjs@isr.ist.utl.pt. Member AIAA.

‡PhD Student, DEEC, Av. Rovisco Pais 1; dcabecinhas@isr.ist.utl.pt.

§PhD Student, DEEC, Av. Rovisco Pais 1; rcunha@isr.ist.utl.pt.

maneuver starts, the ILS guides the vehicle to a certain height, referred to as the decision height, which depends on the airport's ILS category and on the ILS based guidance system available onboard the aircraft. Different ILS categories provide different levels of autonomy to the aircraft runway approach and landing system. The most advanced one, ILS Category IIIc, allows for the automatization of the entire maneuver including guidance along the runway. Despite the availability of those advanced landing systems, their complexity and the high cost involved on their implementation turn them into prohibitive solutions for small UAVs which should be able to land on any opportunity runway, grassy strip, or available road, resorting to low cost onboard navigation systems.[5] These systems provide the vehicle's automatic landing guidance and control algorithms with the actual vehicle's linear and angular positions and velocities, and dedicated modules allow for the integration of GPS/INS information with height data as acquired by a Radar Altimeter or Laser Range Finder mounted underneath the aircraft.

In this paper, the autolanding guidance and control problem is addressed along the lines of the work reported in Refs. 6, 7, and in a companion paper on path following control for coordinated turn maneuvers, Ref. 8, while having in mind the high precision requirements involved in the design of guidance and control laws for the terminal approach and landing maneuvers of fixed wing aircrafts. The proposed solution to tackle the autolanding guidance and control system design problem is a path-following velocity-tracking technique[9] that relies on the definition of a path-dependent error space to express the dynamic model of the aircraft. The error vector, which the autolanding controller should drive to zero, comprises velocity errors, orientation errors, and the distance to the desired path along the different landing phases, defined as the distance between the actual vehicle's position and its orthogonal projection on the path. For different approaches to the problem, the interested reader is referred to Ref. 10, which discusses a landing angle estimation algorithm in UAV autolanding simulation, Ref. 11, where the authors investigate the use of neural networks with linearized inverse aircraft model in automatic landing systems, and to Ref. 12, that presents a mixed $H_2/H_\infty$ controller design for autolanding systems with application to a commercial airplane.

The design and implementation of high-precision robust guidance and control algorithms is one of the key elements in the development of reliable UAV systems. Several approaches to the problem have been proposed, including robust linear control, nonlinear control, neural networks, and fuzzy control – see for example Refs. 13, 14 and references therein. Nonlinear approaches rely on feedback linearization and backstepping techniques, which require the aircraft dynamic model to be approximated by an input-output linearizable system. Linear Parameter Varying (LPV) models represent nowadays a compromise between the global accuracy of nonlinear models and the straightforward controller synthesis techniques available for Linear Time Invariant (LTI) representations. It is well-known that LPV models used within the framework of gain-scheduling constitute a powerful tool for tackling difficult nonlinear problems.[15,16] In the present design, a polytopic LPV representation with piecewise affine dependence on the parameters is adopted to accurately model the desired aircraft dynamics over a set of predefined operating regions. Using an Linear Matrix Inequalities (LMIs) approach and based on the concept of quadratic stability for LPV systems, this paper addresses the autolanding controller synthesis problem in a systematic way and derives in a straightforward manner $H_2$ controllers for the selected operating regions. The resulting set of nonlinear controllers are implemented resorting to the so called D-methodology[17] thereby eliminating the need to feedforward the trimming values for the actuation signals and outputs.

In order to design and evaluate the performance of the autolanding controller, a simulation model of the aircraft dynamics named *SimAirDyn*, is introduced. *SimAirDyn* implements, in the MATLAB Simulink environment, a dynamic model for fixed wing aircrafts valid over a wide flight envelope. The model was derived from first-principles for effective control system design and simulation. The airplane is modeled as a six degrees of freedom rigid body, actuated by forces and moments that are generated at the propeller, fuselage, wings, empennage and control surfaces. The remaining components, such as the landing gear and the antennas, which have a smaller impact on the overall behavior of the aircraft dynamic model, are not included in the simulator and will be treated as disturbances by the control system. Several reference books on the theory of fixed wing aircraft flight dynamics can be found in the literature. The reader is referred to Ref. 18 and Ref. 19 for a thorough and extensive coverage of full-scale aircraft dynamic modeling. Previous work on aircraft flight dynamics identification can be found in Ref. 20 where the authors treat parameter identification issues for nonlinear multivariable aircraft models and report results on the convergence analysis of the proposed identification algorithm.

The paper is organized as follows. Section II presents *SimAirDyn*, a simulation based on the standard rigid-body dynamic model, which can be used to describe autonomous air vehicles; Section III introduces

the path-dependent error space for each stage of the landing maneuver, presents a derivation of the error dynamics parameterized by a vector that fully characterizes the desired operating point, and particularizes for the case of airplanes, introducing a reduced parameter vector and a suitable error output vector; Section IV reviews theoretical results on LPV systems and presents the strategy adopted to guide and control the vehicle; simulation results obtained with the full nonlinear model of an UAV are presented in Section V.

## II. Vehicle Dynamic Model

This section presents an airplane dynamic model referred to as *SimAirDyn* and particularizes it for the model-scale aircraft depicted in Figure 1. A comprehensive study of the aircraft dynamics can be found in Ref. 18. For an in-depth coverage of aircraft flight dynamics, the reader is also referred to Ref. 19. *SimAirDyn* is an accurate mathematical model which was developed for effective control system design and flight envelope expansion. The aircraft is modeled as a six degrees of freedom rigid body, actuated by forces and moments, generated at the propeller, fuselage, empennage, wings, and control surfaces.[18,19,21] The remaining components, that include the landing gear and the antennas, have a smaller impact on the overall behavior of the aircraft dynamics, are not modeled in the simulator, and will naturally be treated as disturbances by the control system. Next, the derivation of *SimAirDyn* is presented.

**Figure 1. Model-scale airplane**

To derive the aircraft equations of motion, the following notation is required. Let $\{I\}$ denote the inertial frame and $\{B\}$ the body frame, attached to the vehicle's center of mass (CM), with $x$-axis pointing to the front of the aircraft, $y$-axis to the right wing and $z$-axis downwards. Let $\left({}^{I}\mathbf{p}_{B},\ {}^{I}_{B}\mathbf{R}\right) \in SE(3) \triangleq \mathbb{R}^3 \times SO(3)$ denote the configuration of $\{B\}$ with respect to $\{I\}$ and $\boldsymbol{\lambda}_B = [\phi_B, \theta_B, \psi_B]^T$, $\theta_B \in \,]-\pi/2, \pi/2[$, $\phi_B$, $\psi_B \in \mathbb{R}$ denote the Z-Y-X Euler angles, representing the attitude of $\{B\}$ relative to $\{I\}$.[22] The rotation matrix ${}^{I}_{B}\mathbf{R}$ and the Euler angles $\boldsymbol{\lambda}_B$ satisfy

$$
\begin{aligned}
{}^{I}_{B}\mathbf{R} = \mathbf{R}_Z(\psi_B)\mathbf{R}_Y(\theta_B)\mathbf{R}_X(\phi_B) \Leftrightarrow \boldsymbol{\lambda}_B &= \arg({}^{I}_{B}\mathbf{R}) \\
&\Leftrightarrow \begin{cases} \theta_B &= \text{atan2}(-r_{31}, \sqrt{r_{11}^2 + r_{21}^2}) \\ \phi_B &= \text{atan2}(r_{32}, r_{33}) \\ \psi_B &= \text{atan2}(r_{21}, r_{11}) \end{cases}, \qquad (1)
\end{aligned}
$$

where atan2(.,.) denotes the four quadrant arctangent function and $\mathbf{R}_Z(.)$, $\mathbf{R}_Y(.)$, and $\mathbf{R}_X(.)$ denote rotation matrices about the $z$, $y$, and $x$ axes, respectively.

Consider also the linear and angular body velocities, $\mathbf{v}_B = [u, v, w]^T$ and $\boldsymbol{\omega}_B = [p, q, r]^T \in \mathbb{R}^3$, given respectively by $\mathbf{v}_B = {}^{B}_{I}\mathbf{R}\,({}^{I}\dot{\mathbf{p}}_B - {}^{I}\mathbf{v}_W)$ and $\boldsymbol{\omega}_B = {}^{B}_{I}\mathbf{R}\,{}^{I}\boldsymbol{\omega}_B$, where ${}^{I}\boldsymbol{\omega}_B \in \mathbb{R}^3$ is the angular velocity of $\{B\}$ with respect to $\{I\}$, and $\mathbf{v}_W$ is the wind velocity relative to $\{I\}$ assumed constant in the present section.

According to this notation, the standard equations for the vehicle's kinematics[22] can be written as

$$\begin{cases} {}^{I}\dot{\mathbf{p}}_{B} = {}^{I}_{B}\mathbf{R}\,\mathbf{v}_{B} + \mathbf{v}_{W} \\ \dot{\boldsymbol{\lambda}}_{B} = \mathbf{Q}(\phi_{B},\,\theta_{B})\,\boldsymbol{\omega}_{B} \end{cases}, \tag{2}$$

where

$$\mathbf{Q}(\phi_{B},\,\theta_{B}) = \begin{bmatrix} 1 & \sin\phi_{B}\tan\theta_{B} & \cos\phi_{B}\tan\theta_{B} \\ 0 & \cos\phi_{B} & -\sin\phi_{B} \\ 0 & \sin\phi_{B}/\cos\theta_{B} & \cos\phi_{B}/\cos\theta_{B} \end{bmatrix}, \tag{3}$$

and the derivative of ${}^{I}_{B}\mathbf{R}$ is given by

$${}^{I}_{B}\dot{\mathbf{R}} = {}^{I}_{B}\mathbf{R}\,\mathbf{S}(\boldsymbol{\omega}_{B}), \tag{4}$$

where $\mathbf{S}(\mathbf{x}) \in \mathbb{R}^{3\times 3}$ is a skew symmetric matrix such that $S(\mathbf{x})\,\mathbf{y} = \mathbf{x} \times \mathbf{y}$, for all $\mathbf{x},\,\mathbf{y} \in \mathbb{R}^{3}$. The dynamic model of the vehicle can be written as

$$\begin{cases} \dot{\mathbf{v}_{B}} = \mathbf{f}(\mathbf{v}_{B}, \boldsymbol{\omega}_{B}, \mathbf{u}, \theta_{B}, \phi_{B}) \\ \dot{\boldsymbol{\omega}_{B}} = \mathbf{n}(\mathbf{v}_{B}, \boldsymbol{\omega}_{B}, \mathbf{u}, \theta_{B}, \phi_{B}) \end{cases}, \tag{5}$$

where $\mathbf{f},\,\mathbf{n} : (\mathbb{R}^{3}, \mathbb{R}^{3}, \mathbb{R}^{m}, \mathbb{R}, \mathbb{R}) \to \mathbb{R}^{3}$ are continuously differentiable functions of the body velocities, attitude and control inputs $\mathbf{u} \in \mathbb{R}^{m}$ that derive from the remaining forces and moments acting on the body. Further define the aircraft airspeed, $V$, the angle-of-attack, AOA, $\alpha = \arctan(w/u)$, and the angle of sideslip $\beta = \arcsin(v/V)$.

The overall model resulting from the integration of the above mentioned components is a highly coupled MIMO nonlinear dynamic system. However, analysis of the mission objectives will help to establish the relevant flight regimes, such as forward flight, coordinated turn, take-off, and landing, whose independent modeling can yield simpler and more effective and intuitive dynamic systems. This paper will give particular focus to the landing maneuver.

A standard procedure in the literature is to separate the aircraft into longitudinal and lateral-directional dynamics. This manipulation leads to a simpler analysis and to a clearer and intuitive interpretation of the results. The full derivation of the longitudinal and lateral-directional dynamics can be found in Ref. 18.

### A. Aircraft Model Description

The resulting dynamic systems for both the full nonlinear model and the simplified models are expressed in state-space form and were used to develop a realistic aircraft simulation model using MATLAB/Simulink. The simplified models for the different flight regimes were validated against the full nonlinear aircraft simulation model, providing the working ground for the control design phase.

The aircraft nonlinear simulation model *SimAirDyn* was properly tuned so that it captures the essential behavior of the actual vehicle for a large operational flight envelope.[18,19] The most important model parameters are the dimensionless aerodynamic force and torque coefficients, which can be obtained from a Taylor series expansion about selected operating regimes.[19] Typically these values are experimentally obtained in a wind tunnel. Alternatively, software packages exist that allow one to obtain reasonably good approximations of wind-tunnel experiments. One of these software packages is LinAir 4 from Desktop Aeronautics, which was purchased by ISR/IST. LinAir 4 is an aircraft geometry modeler that provides a wide range of computational aerodynamic analysis, based on the calculation of the aerodynamic characteristics of multi-element, nonplanar lifting surfaces. The methodology used to derive the nonlinear dynamic model parameters from the aerodynamic loads estimated by LinAir 4 was based on the relation between the system responses and the relative interplay of physical quantities.

$$\begin{cases} \mathbf{f}(\mathbf{v}_{B}, \boldsymbol{\omega}_{B}, \mathbf{u}_{ad}, \theta_{B}, \phi_{B}) = \mathbf{f}_{ad}(\mathbf{v}_{B}, \boldsymbol{\omega}_{B}, \mathbf{u}_{ad}) + \mathbf{f}_{g}(\theta_{B}, \phi_{B}) + \begin{bmatrix} T & 0 & 0 \end{bmatrix}^{T} \\ \mathbf{n}(\mathbf{v}_{B}, \boldsymbol{\omega}_{B}, \mathbf{u}_{ad}, \theta_{B}, \phi_{B}) = \mathbf{n}_{ad}(\mathbf{v}_{B}, \boldsymbol{\omega}_{B}, \mathbf{u}_{ad}) \end{cases} \tag{6}$$

As expressed in eq. (6), the external forces and moments acting on the rigid body can be separated into gravity, $\mathbf{f}_{g}(\theta_{B}, \phi_{B})$, airflow acting on the fuselage, wings, empennage and control surfaces, $\mathbf{f}_{ad}(\mathbf{v}_{B}, \boldsymbol{\omega}_{B}, \mathbf{u}_{ad})$

and $\mathbf{n}_{ad}(\mathbf{v}_B, \boldsymbol{\omega}_B, \mathbf{u}_{ad})$, and the force exerted by the propeller $[T, 0\,0]^T$. The gravitational terms can be trivially computed from the attitude of the aircraft, while the remaining ones were obtained using a least square fitting from data generated by LinAir 4. In (6), $\mathbf{u}_{ad} = [\delta_{a_L}, \delta_{a_R}, \delta_r, \delta_e, \delta_f]^T$ represents the vector of control inputs, where $\delta_{a_L}, \delta_{a_R}, \delta_r, \delta_e, \delta_f$ are the deflection angles of left and right ailerons, rudder, elevator, and flaps, respectively. The main problems addressed were the development of a reliable strategy for nonlinear model structure and parameter identification from data produced by LinAir 4 and the selection of a set of aircraft maneuvers and control surface configurations to cover the aircraft flight envelope. The aerodynamic forces and moments acting on the airframe were evaluated for several flight conditions and then interpolated using a least square fitting to obtain the aircraft dynamic model for the whole flight envelope.

The model was tuned for the aircraft presented in Figure 1. This aircraft is capable of lifting a 11 kg payload for two hours on a tank of gas. The wingspan is 3.5 m and the length is 1.8 m, and it has a takeoff distance half loaded of 50 m. It uses a one cylinder two stroke-60 cc engine, producing about 8 horsepower.

For the nonlinear simulation model to match the actual aircraft actuators, rate limitations and saturation were included. The rate limitation is modeled using the system depicted in Figure 2, where $\alpha_a = 50$ rad/s. The rate limit is $\alpha_a k = 7$ rad/s for the control surfaces, and $\alpha_a k = 10$ N/s for the thrust. The saturation of actuators was set to $\pm 30$ degrees for the surfaces and 110 N for the thrust generated by the propeller. In the figure, $u_r$ is the reference control input and $u$ is the corresponding rate limited control signal applied to the aircraft.

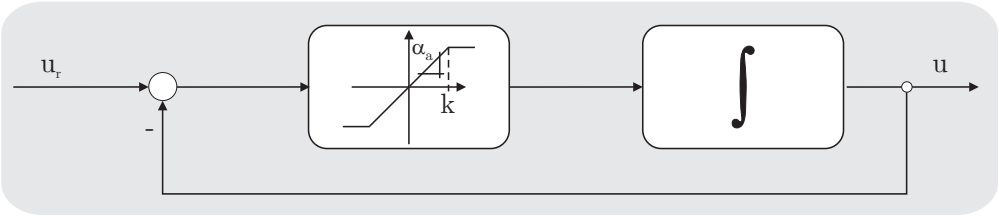


**Figure 2. Rate limitation system for the actuators**

## B. Model Analysis

A standard approach followed in aircraft stability analysis assumes that the coupling between lateral-directional and longitudinal modes can be neglected, and that, for a given flight condition, the airplane motion can be described by two independent lower-order linear systems.

### *1. Longitudinal Dynamics*

Let $\mathbf{x}_{long}(t) = [u(t)/V_0\ \alpha(t)\ q(t)\ \theta_B(t)]^T$ denote the vector of incremental longitudinal state variables about equilibrium trajectories, where $V_0$ is the steady-state airspeed given by $V_0 = \sqrt{u_0^2 + v_0^2 + w_0^2}$, $\alpha$ the AOA, $q$ the pitch angle rate, and $\theta_B$ the pitch angle that describes the rotation of the airplane about the $y$-axis of the body frame. After linearizing the longitudinal dynamics, one obtains

$$\dot{\mathbf{x}}_{long}(t) = \mathbf{A}_{long}\mathbf{x}_{long}(t) + \mathbf{B}_{long}\boldsymbol{\delta}_{Long}(t) \tag{7}$$

where $\boldsymbol{\delta}_{Long} = [T, \quad \delta_{a_C}, \quad \delta_f, \quad \delta_e]^T$ is the vector of incremental longitudinal control inputs. $T$ is the thrust generated by the propeller, $\delta_{a_C}$ is referred to as the common-mode of the ailerons, $\delta_f$ is the flaps deflection angle and $\delta_e$ is the elevator deflection angle. The common-mode of the ailerons is defined as

$$\delta_{a_C} = \frac{\delta_{a_L} + \delta_{a_R}}{2} \tag{8}$$

where $\delta_{a_L}$ and $\delta_{a_R}$ are the left and right ailerons incremental deflection angles, respectively.

The eigenvalues of $\mathbf{A}_{long}$ typically form two pairs of complex conjugate poles and define two natural modes for the system. Using the standard notation, these can be described by

$$\lambda = -\omega_n\xi \pm \omega_n\sqrt{1-\xi^2}$$

where $\omega_n$ is the natural frequency of the mode and $\xi$ the damping coefficient. The fastest mode affects mostly the AOA and the pitch angle of the vehicle, with major impact on the states $\alpha$, $\theta_B$ and $q$. When excited, this mode takes only a few seconds to reach steady-state and depends mainly on the relative location of the center of mass (CM) of the airplane and its neutral point (NP). The NP is the virtual location where the CM should be for the aircraft to have neutral longitudinal stability. It can be shown that if the NP is located aft of the CM, then the airplane is longitudinally stable.[18]

The slowest mode, commonly referred to as phugoid, affects mainly the normalized longitudinal velocity $u/V_0$, and the pitch angle $\theta_B$. The AOA and the pitch rate remain almost unchanged. Since $q$ is near zero, this mode is usually called the slow longitudinal mode. This mode can be physically interpreted as an oscillation on the altitude of the aircraft with cyclic transfers between kinetic energy and potential energy.

For the aircraft illustrated in Figure 1, the linearized model obtained when the vehicle describes a straight line path, at a speed of 30 m/s, has the fastest mode with frequency 14.31 rad/s and damping coefficient of 0.95. The phugoid mode is characterized by a frequency of 0.32 rad/s, which corresponds to a period of about 19.6 s, and a damping coefficient of 0.1.

*2. Lateral-Directional Dynamics*

For the lateral-directional dynamics, the incremental state vector can be defined as

$$\mathbf{x}_{ld}(t) = [\beta(t)\ p(t)\ \phi_B(t)\ r(t)]^T \tag{9}$$

where $\beta$ is the angle of sideslip, $\phi_B$, the roll angle, $p = \dot{\phi_B}$ and $r = \dot{\psi_B}$, the roll and yaw rates, respectively. For the sake of completeness, we can write

$$\dot{\mathbf{x}}_{ld}(t) = \mathbf{A}_{ld}\mathbf{x}_{ld}(t) + \mathbf{B}_{ld}\boldsymbol{\delta}_{ld}(t) \tag{10}$$

where $\boldsymbol{\delta}_{ld} = [\delta_{a_D}, \delta_r]^T$ is the vector of incremental longitudinal control inputs, $\delta_{a_D}$ is the differential-mode of the ailerons given by eq. 11, and $\delta_r$ is the rudder angle.

$$\delta_{a_D} = \frac{\delta_{a_L} - \delta_{a_R}}{2} \tag{11}$$

The lateral-directional dynamics is known to have one pair of complex conjugate poles and two poles on the real axis. The fastest of the real poles can be related to the roll angle, $\phi_B$, affecting mainly this state and its derivative, $p$. Therefore, this mode describes a pure roll maneuver, since all other states remain unchanged. The other real pole is related to the spiral mode. In some airplanes, this mode is unstable leading the aircraft to naturally enter into a decreasing radius spiral trajectory.

The remaining pair of complex conjugate poles is associated with the so-called Dutch-roll mode. For this mode, it can be shown that the sideslip and the yaw angles have a phase difference close to 180 degrees. This is reasonable from a physical point of view since, along an equilibrium trajectory, if the yaw angle suffers a disturbance, then it will also generate a sideslip angle disturbance with opposite sign, due to the definition of angle $\beta$. In fact, this generates an oscillatory movement of the CM about a straight line defined by the mean velocity of the airplane, together with a roll motion induced by the airflow asymmetry on the aircraft wings created by a nonzero sideslip angle.

Using the same trimming condition as before, a pure roll mode with a frequency of 205 rad/s was identified. The Dutch-roll mode was found with a frequency of 11.8 rad/s and a damping coefficient of 0.14 and a slower unstable eigenvalue with frequency 0.023 rad/s was associated to the spiral mode.

### C. Flaps

The flaps constitute a special type of actuators that are commonly used in manned airplanes during the landing phase. They are control surfaces placed on the wings, usually near the fuselage, with objective of extending the wings' chord. This increases both the lift and the drag forces acting on the airplane, allowing for lower speed flight trajectories. Although they are important on large aircrafts, they are not necessarily employed in smaller ones.

Since flaps are very slow control surfaces when compared to the rest of the aircraft actuators, they must be treated differently. In the present case study, they will be used in a stepwise manner, as a function of the aircraft's height. This corresponds to the standard technique used in manned aircrafts.

## III. Path-dependent Error Dynamic Model

The main objective of the present work is the design of a controller to steer the aircraft along the final approach phase which is associated with a smooth three-dimensional curve denoted by $\Gamma$. During this phase, the aircraft aligns itself with the runway and stabilizes about a constant sink rate and decreasing velocity maneuver, called glideslope, until the flare maneuver brings it to touchdown. In this section, we present the transformation applied to the aircraft dynamics (5) to obtain an error dynamic model, which will then be used to design controllers both for the glideslope and flare maneuvers.

### A. Coordinate Frames

In order to define this error space, we must first introduce two coordinate frames relating the vehicle and the desired path $\Gamma$. These are the tangent frame $\{T\}$ and the desired body frame $\{C\}$ shown in Figure 3. Both coordinate frames move along the reference path attached to the point on the path closest to the vehicle. The difference between the two lies in the fact that $\{T\}$ is always aligned with the tangent to the path, whereas $\{C\}$ gives the desired body orientation, which typically does not coincide with the tangent to the path. There is a correspondence between $\{T\}$ and the standard Serret-Frenet frame, formed by the tangent, normal, and binormal vectors. Both frames share the same $x$-axis, the tangent vector, and have collinear $y$ and $z$ axes. Following Ref. 23, while in the Serret-Frenet frame the normal always points "inside" the curve, this may not be case with the $\{T\}$ frame, whose $z$-axis points always downwards. This property widens the set of curves for which continuity in the $\{T\}$ frame can be guaranteed.

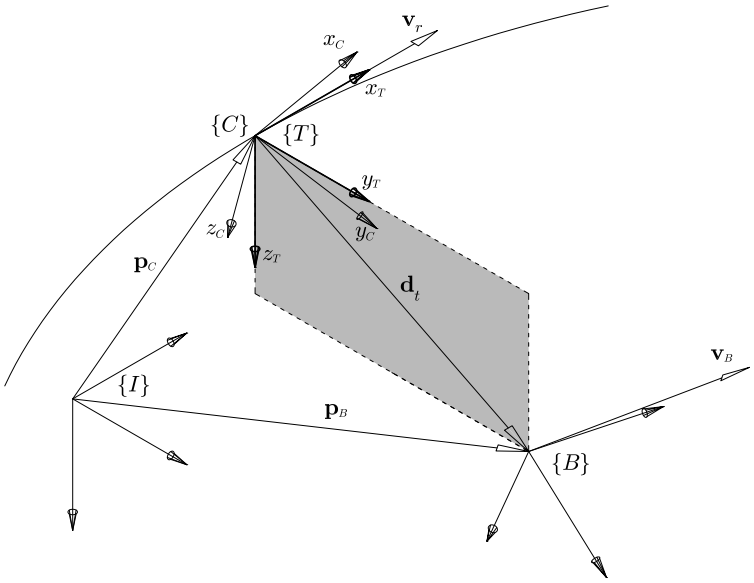


**Figure 3. Coordinate frames $\{T\}$, $\{B\}$ and $\{I\}$**

### B. Error Space Definition

We define the vector $\mathbf{d}$ as the distance between the origin of the aircraft body frame $\{B\}$ and the closest point on the desired path, which can be expressed in the inertial coordinate frame as

$$\mathbf{d} = {}^{I}\mathbf{p}_{B} - {}^{I}\mathbf{p}_{T} \tag{12}$$

where $\mathbf{p}_T$ represents the origin of frame $\{T\}$. Writing $\mathbf{d}$ in the coordinates of frame $\{T\}$ results in a vector with null $x$-axis component given by

$${}^{T}\mathbf{d} = {}^{T}\mathbf{p}_{B} - {}^{T}\mathbf{p}_{T} = {}^{T}_{I}\mathbf{R}\left({}^{I}\mathbf{p}_{B} - {}^{I}\mathbf{p}_{T}\right) = \begin{bmatrix} 0 \\ \mathbf{d}_{T} \end{bmatrix} = \begin{bmatrix} 0 \\ d_y \\ d_z \end{bmatrix}. \tag{13}$$

The linear and angular velocities of frame $\{T\}$ relative to the inertial frame, expressed in $\{T\}$, are given by ${}^{T}({}^{I}\mathbf{v_T}) = \mathbf{v}_T = \begin{bmatrix} V_T & 0 & 0 \end{bmatrix}^T$ and ${}^{T}({}^{I}\boldsymbol{\omega}_T) = \boldsymbol{\omega}_T = V_T \begin{bmatrix} \tau & 0 & k \end{bmatrix}^T$, respectively, where $V_T$ is the linear speed, and $\kappa$ and $\tau$ are trajectory parameters defined in Ref. 9. Using these expressions and taking the time derivative of vector $\mathbf{d}_T$ one obtains

$$\begin{aligned} \begin{bmatrix} 0 \\ \dot{\mathbf{d}}_T \end{bmatrix} &= \dot{{}^{T}_{I}\mathbf{R}}\left({}^{I}\mathbf{p}_B - {}^{I}\mathbf{p}_T\right) + {}^{T}_{I}\mathbf{R}\left({}^{I}\dot{\mathbf{p}}_B - {}^{I}\dot{\mathbf{p}}_T\right) = -\mathbf{S}(\boldsymbol{\omega}_T)\begin{bmatrix} 0 \\ \mathbf{d}_T \end{bmatrix} + {}^{T}_{I}\mathbf{R}\,{}^{I}_{B}\mathbf{R}\mathbf{v}_B - {}^{T}_{I}\mathbf{R}\,{}^{I}_{T}\mathbf{R}\mathbf{v}_T \\ &= -\mathbf{S}\left(V_T \begin{bmatrix} \tau \\ 0 \\ k \end{bmatrix}\right)\begin{bmatrix} 0 \\ \mathbf{d}_T \end{bmatrix} + {}^{T}_{B}\mathbf{R}\mathbf{v}_B - \begin{bmatrix} V_T \\ 0 \\ 0 \end{bmatrix} = -V_T \begin{bmatrix} -k\,d_y \\ -\tau\,d_z \\ \tau\,d_y \end{bmatrix} + {}^{T}_{B}\mathbf{R}\mathbf{v}_B - \begin{bmatrix} V_T \\ 0 \\ 0 \end{bmatrix} \end{aligned}, \tag{14}$$

and consequently

$$V_T = \frac{1}{1 - k\,d_y}\begin{bmatrix} 1 & 0 & 0 \end{bmatrix}{}^{T}_{B}\mathbf{R}\mathbf{v}_B. \tag{15}$$

In order to ensure that the vehicle not only follows a predefined curve $\Gamma$ but also tracks a given velocity profile, as is mandatory for the kind of maneuvers considered in the present paper, extra reference signals are needed. For that purpose, we consider the reference tangent speed $V_r$, which defines references for both the linear and angular tangent velocities given by

$$\mathbf{v}_r = V_r \begin{bmatrix} 1 \\ 0 \\ 0 \end{bmatrix} = \frac{V_r}{V_T}\mathbf{v}_T \qquad\qquad \boldsymbol{\omega}_r = \frac{V_r}{V_T}\boldsymbol{\omega}_T, . \tag{16}$$

respectively. The desired orientation can be represented by the Z-Y-X Euler angles $\boldsymbol{\lambda}_C = [\phi_C\ \theta_C\ \psi_C]^T$, $\theta_C \in\, ]-\pi/2, \pi/2[\,,\ \phi_C, \psi_C \in \mathbb{R}$. Given the definitions of $\{T\}$, $\{C\}$, and references $\mathbf{v}_r$ and $\boldsymbol{\omega}_r$, we introduce the following error state vector

$$\mathbf{x}_e = \begin{bmatrix} \mathbf{v}_e \\ \boldsymbol{\omega}_e \\ \mathbf{d}_T \\ \boldsymbol{\lambda}_e \end{bmatrix} = \begin{bmatrix} \mathbf{v}_B - {}^{B}_{T}\mathbf{R}\mathbf{v}_r \\ \boldsymbol{\omega}_B - {}^{B}_{T}\mathbf{R}\boldsymbol{\omega}_r \\ \begin{bmatrix} 0 & 1 & 0 \\ 0 & 0 & 1 \end{bmatrix}{}^{T}_{I}\mathbf{R}\left({}^{I}\mathbf{p}_B - \mathbf{p}_C\right) \\ \boldsymbol{\lambda}_B - \boldsymbol{\lambda}_C \end{bmatrix}, \tag{17}$$

where the states $\mathbf{v}_e$ and $\boldsymbol{\omega}_e$ are used for velocity profile tracking, while the distance $\mathbf{d}_T$ allows for path-following. Finally, the error $\boldsymbol{\lambda}_e$ is used to obtain aircraft attitude convergence. ¿From eq. (17), it is straightforward to observe that the aircraft follows the path ($\mathbf{d}_T = 0$) with the linear speed $\|\mathbf{v}_B\| = V_T = V_T$ and orientation $\boldsymbol{\lambda}_B = \boldsymbol{\lambda}_C$ if and only if $\mathbf{x}_e = \mathbf{0}$.

Under these constraints, the error dynamics[24] can be written as

$$\begin{cases} \dot{\mathbf{v}}_e = \dot{\mathbf{v}}_B + \mathbf{S}(\boldsymbol{\omega}_e)\,{}^{B}_{T}\mathbf{R}\,\mathbf{v}_r + \left(1 - \dfrac{V_T}{V_r}\right){}^{B}_{T}\mathbf{R}S(\boldsymbol{\omega}_r)\,\mathbf{v}_r \\ \dot{\boldsymbol{\omega}}_e = \dot{\boldsymbol{\omega}}_B + S(\boldsymbol{\omega}_e)\,{}^{B}_{T}\mathbf{R}\,\boldsymbol{\omega}_r \\ \dot{\mathbf{d}}_T = V_T\tau\begin{bmatrix} 0 & 1 \\ -1 & 0 \end{bmatrix}\mathbf{d}_T + \begin{bmatrix} 0 & 1 & 0 \\ 0 & 0 & 1 \end{bmatrix}{}^{T}_{B}\mathbf{R}\,\mathbf{v}_e \\ \dot{\boldsymbol{\lambda}}_e = Q(\phi_B, \theta_B)\boldsymbol{\omega}_B - \mathrm{sign}(\kappa)V_T\sqrt{\kappa^2 + \tau^2}[0\ 0\ 1]^T \end{cases}. \tag{18}$$

The set of allowable paths is now restricted to the set of trimming paths. Similarly, the reference speed, $V_r$, and the motion of $\{C\}$ are constrained to correspond to trimming trajectories consistent with the chosen path. A trimming path corresponds to a curve that the aircraft can follow while satisfying the trimming condition, which is equivalent to having $\dot{\mathbf{v}}_B = 0$, $\dot{\boldsymbol{\omega}}_B = 0$, and $\dot{\mathbf{u}} = 0$ in (5). It is well known that, for a vehicle with dynamics described by (5) and assuming constant gravitational acceleration, the set of trimming trajectories comprises all $z$-aligned helices and straight-line trajectories. In the application presented here,

the aircraft is expected to track trajectories in the vertical plane with no sideslip, which correspond to the glideslope and flare maneuvers, reducing the allowed trimming paths to vertical plane straight lines. Under these assumptions, the desired flight envelope can be parameterized by the vector $\boldsymbol{\xi} = (V_r,\, \theta_T,\, \theta_C,\, \delta_f)$, where $\theta_T$ is the well known flight path angle $\gamma$, $\theta_C$ the aircraft pitch angle, and $\delta_f$ the deflection of the flaps.

To accomplish the tracking objectives during the sensitive landing maneuvers we define an output vector $\mathbf{y}_e$ that corresponds to a combination of error components expressed on the body coordinate system, to be driven to zero at steady-state by means of integral action. To summarize the foregoing considerations, the error dynamic system for an aircraft can be written as

$$\mathcal{P}(\boldsymbol{\xi}) := \begin{cases} \dot{\mathbf{x}}_e = \mathbf{f}_e(\mathbf{x}_e, \mathbf{u}, \boldsymbol{\xi}) \\ \mathbf{y} = \mathbf{g}(\mathbf{x}_e, \boldsymbol{\xi}) \end{cases}, \tag{19}$$

where the output to be integrated satisfies, for allowed values of $\boldsymbol{\xi} = \boldsymbol{\xi}_0$, $\mathbf{g}(\mathbf{0}, \boldsymbol{\xi}_0) = \mathbf{0}$. Recalling that $\boldsymbol{\xi}$ is a constant parameter vector, the linearization of $\mathcal{P}(\boldsymbol{\xi})$ about $(\mathbf{x}_e = 0,\, \mathbf{u} = \mathbf{u}_\xi)$ results in a time-invariant system of the form

$$\mathcal{P}_l(\boldsymbol{\xi}) = \begin{cases} \delta\dot{\mathbf{x}}_e = A_e(\boldsymbol{\xi})\delta\mathbf{x}_e + B_e(\boldsymbol{\xi})\delta\mathbf{u} \\ \delta\mathbf{y}_e = C_e(\boldsymbol{\xi})\delta\mathbf{x}_e \end{cases}, \tag{20}$$

where $A_e(\boldsymbol{\xi}) = \dfrac{\partial \mathbf{f}_e}{\partial \mathbf{x}_e}(0, \mathbf{u}_\xi, \boldsymbol{\xi})$, $B_e(\boldsymbol{\xi}) = \dfrac{\partial \mathbf{f}_e}{\partial \mathbf{u}}(0, \mathbf{u}_\xi, \boldsymbol{\xi})$, and $C_e(\boldsymbol{\xi}) = \dfrac{\partial \mathbf{g}}{\partial \mathbf{x}_e}(0, \boldsymbol{\xi})$.

## IV. Controller Synthesis

Aircraft dynamic models are complex nonlinear systems that are in general functions of the dynamic pressure and angles of attack and side-slip. Hence, it is inadequate, for control purposes, to represent them by LTI models. Linear Parameter Varying models embody nowadays a compromise between the global accuracy of nonlinear models and the straightforward controller synthesis techniques available for LTI representations. These parameter dependent systems arise naturally while modeling physical systems, where the corresponding state space description depends on a set of parameters. In the present work, a piecewise affine dependence on the parameters will be considered to accurately model the error dynamics over a wide flight-envelope. The identification of LPV models, given the model structure and order, is addressed determining the number of local models, the set of operating points, and the set of variables that can be used to form the scheduling vector.

In the approach pursued in this paper, results presented in Refs. 25, 26 were used to develop the LMI based controller synthesis algorithm for affine parameter dependent systems. Much of the work in this area is well rooted in the theory of LMIs, which provide a powerful formulation framework as well as a versatile design technique for a wide variety of linear control problems. Since solving LMIs is a convex optimization problem for which efficient numerical solvers are now available, an LMI based formulation can be seen as a practical solution for many control problems.

### A. Design Specifications

The linear controllers for the glideslope and flare maneuvers are required to meet the following design specifications:

*Zero Steady State Error.* Achieve zero steady state values for the distance to the reference path, the linear velocity error, and the roll angle.

*Bandwidth Requirements.* The input-output command response bandwidth for the path following error channels should be on the order of 0.1 rad/s; the control loop bandwidth for the deflection surfaces channels should not exceed 5 rad/s, to ensure that the actuators would not be driven beyond their normal actuation bandwidth.

*Closed Loop Damping and Stability Margins.* The closed loop eigenvalues should have a damping ratio of a least 0.7 and a magnitude of at least 0.1 rad/s.

*Glideslope.* In this phase of the maneuver it will be required to achieve zero steady state deflection of the common mode of the ailerons $\delta_{a_C} = 0$.

*Flare.* In this phase of the landing maneuver, the aircraft should achieve zero steady state error in response to pitch angle commands.

To satisfy the design requirements we introduce the following integral error for the glideslope maneuver

$$\begin{bmatrix} x_1 \\ \mathbf{x}_2 \\ x_3 \end{bmatrix} = \begin{bmatrix} \int \phi_e dt \\ \int \left( \mathbf{v}_e + {}^{B}_{T}\mathbf{R} \left[ 0 \ \mathbf{d}_T^T \right]^T \right) dt \\ \int \delta_{a_C} dt \end{bmatrix} \tag{21}$$

where $\phi_e = \phi_C - \phi_B$. For the flare maneuver, to satisfy the tracking requirements on the aircraft pitch angle we remove the state $x_3$ and introduce a new integral state $x_4$, defined as

$$x_4 = \int \theta_e dt. \tag{22}$$

where $\theta_e = \theta_C - \theta_B$. Two different control objectives have been introduced. The switching between states $x_3$ and $x_4$, requires the use of different controllers, one for each case. Notice that, when the state $x_4$ is selected, the airspeed and pitch references profiles should agree, in order to keep the aircraft control surfaces away from saturation during the controller switching. Furthermore, the reference pitch angle close the touchdown depends on the aircraft weight. When the mass increases, the reference pitch angle should also increase, to produce the required lift force without recruiting the actuators.

## B. Theoretical Background

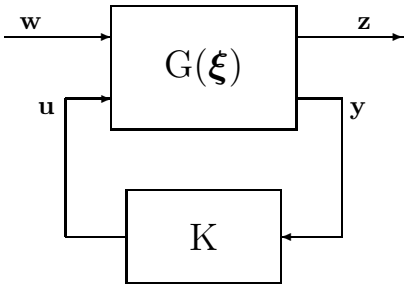


**Figure 4. Feedback interconnection**

In this section an LMI approach is used to tackle the continuous-time state feedback $H_2$ synthesis problem for polytopic LPV systems. Consider the LPV system represented in Figure 4 with realization

$$\mathrm{G}(\boldsymbol{\xi}) = \begin{cases} \dot{\mathbf{x}} = A(\boldsymbol{\xi})\mathbf{x} + B_w(\boldsymbol{\xi})\mathbf{w} + B(\boldsymbol{\xi})\mathbf{u} \\ \mathbf{z} = C(\boldsymbol{\xi})\mathbf{x} + D(\boldsymbol{\xi})\mathbf{w} + E(\boldsymbol{\xi})\mathbf{u} \end{cases}, \qquad \mathbf{u}(t) = \mathrm{K}\mathbf{y}(t), \tag{23}$$

where $\mathbf{x}$ is the state vector, $\mathbf{w}$ denotes the input vector of exogenous signals (including commands and disturbances), $\mathbf{z}$ is the output vector of errors to be reduced, $\mathbf{y}$ is the vector of measurements that are available for feedback, which in the present case coincide with $\mathbf{x}$, and $\mathbf{u}$ is the vector of actuator signals. The generalized plant $\mathrm{G}(\boldsymbol{\xi})$ consists of the augmented system described before together with weights that shape the exogenous and internal signals. The system G is parameterized by $\boldsymbol{\xi}$, which is a possibly time-varying parameter vector and belongs to the convex set $\Xi = \mathrm{co}(\Xi_0)$ where $\mathrm{co}(\cdot)$ denotes the convex hull.

Since the synthesis problem involves testing an infinite number of LMIs, several different structures for the LPV system have been proposed which reduce the problem to that of solving a finite number of LMIs. In this work, we have adopted a polytopic description, which can be used to model a wide spectrum of systems and, as shown in the paper, is an adequate choice for the system at hand.

**Definition IV.1** (Polytopic LPV system)**.** The system (23) is said to be a polytopic LPV system with affine parameter dependence if the system matrix

$$S(\boldsymbol{\xi}) = \begin{bmatrix} A(\boldsymbol{\xi}) & B_w(\boldsymbol{\xi}) & B(\boldsymbol{\xi}) \\ C(\boldsymbol{\xi}) & D(\boldsymbol{\xi}) & E(\boldsymbol{\xi}) \end{bmatrix} \tag{24}$$

verifies $S(\boldsymbol{\xi}) = S^{(0)} + \sum_{j=1}^{n_p} S^{(j)}\xi_j$, for all $\boldsymbol{\xi} = [\xi_1 \dots \xi_{n_p}]^T \in \Xi$, and the parameter set takes the form $\Xi = \mathrm{co}(\Xi_0)$, where

$$\Xi_0 = \{\boldsymbol{\xi} \in \mathbb{R}^{n_p} |\ \xi_i \in \{\underline{\xi}_i, \overline{\xi}_i\},\ \underline{\xi}_i \leq \overline{\xi}_i,\ i = 1, \dots, n_p\}\ .$$

We are interested in finding a solution to the continuous-time state feedback $H_2$ synthesis problem. Consider the static state feedback law given by $\mathbf{u} = K\mathbf{x}$ and let $T_{zw}$ denote the closed-loop operator from $\mathbf{w}$ to $\mathbf{z}$. Then, the $H_2$ synthesis problem can be described as that of finding a control matrix $K$ that stabilizes the closed-loop system and minimizes the $H_2$ norm $\|T_{zw}\|_2$. Note that matrix $D(\boldsymbol{\xi}) = 0$ in order to guarantee that $\|T_{zw}\|_2$ is finite for every internally stabilizing and strictly proper controller. The technique used for controller design relies on results available in Refs. 27,28, after being rewritten for the case of polytopic LPV systems. In the following, $\mathrm{tr}(L)$ denotes the trace of matrix $L$.

**Result IV.1.** *A static state feedback controller guarantees the $\zeta$ upper-bound for the continuous-time $H_2$ norm of the closed-loop operator $T_{zw}(\boldsymbol{\xi})$ for all $\boldsymbol{\xi} \in \Xi$, that is,*

$$\|T_{zw}(\boldsymbol{\xi})\|_2 < \zeta, \forall \boldsymbol{\xi} \in \Xi \tag{25}$$

*if there are real matrices $X = X^T > 0$, $Y > 0$, and $W$ such that*

$$\begin{bmatrix} A(\boldsymbol{\xi})\,X + X\,A(\boldsymbol{\xi})^T + B(\boldsymbol{\xi})\,W + W^T\,B(\boldsymbol{\xi})^T & B_w(\boldsymbol{\xi}) \\ B_w(\boldsymbol{\xi})^T & -I \end{bmatrix} < 0 \tag{26a}$$

$$\begin{bmatrix} Y & C(\boldsymbol{\xi})\,X + E(\boldsymbol{\xi})\,W \\ X\,C(\boldsymbol{\xi})^T + W^T\,E(\boldsymbol{\xi})^T & X \end{bmatrix} > 0 \tag{26b}$$

$$\mathrm{tr}\,(Y) < \zeta^2\ . \tag{26c}$$

*for all $\boldsymbol{\xi} \in \Xi_0$. The respective controller gain matrix is given by $K = W\,X^{-1}$.*

Additional closed-loop regional eigenvalues placement specifications for each plant $G(\boldsymbol{\xi})$ in the polytopic region can also be converted into design constraints resorting to the concept of LMI regions in the complex plane introduced in Ref. 29. These constitute a generalization of the well known $\alpha$-stability region presented next.

**Result IV.2.** *The closed-loop system with realization* (23) *has all the eigenvalues in the semi-plane $\lambda \in \mathbb{C}$ : $Re(\lambda) < -\alpha$ for all $\boldsymbol{\xi} \in \Xi$ if matrices $X = X^T > 0$ and $W$ exist such that the closed-loop Lyapunov inequality*

$$A(\boldsymbol{\xi})\,X + X\,A(\boldsymbol{\xi})^T + B(\boldsymbol{\xi})\,W + W^T\,B(\boldsymbol{\xi})^T + 2\alpha I < 0 \tag{27}$$

*is satisfied for all $\boldsymbol{\xi} \in \Xi_0$.*

This well known result can be generalized as follows. Let $L = [l_{ij}]$ and $M = [m_{ij}]$ be real symmetric matrices. An LMI region $\mathrm{R}_{lmi}$ is defined as an open domain in the complex plane that satisfies

$$\mathrm{R}_{lmi} = \{z \in \mathbf{C} : l_{ij} + m_{ij}z + m_{ji}\bar{z} < 0; \qquad i, j = 1, ..., n\}\,. \tag{28}$$

This description can represent a large number of regions which are symmetric with respect to the real axis, such as conic sectors, half-planes, etc. Using the concept of LMI regions, Result IV.2 admits the following generalization[29]

**Result IV.3.** *The closed-loop system with realization* (23) *has all the eigenvalues in the region $\mathrm{R}_{cl}$ defined by* (28) *for all $\boldsymbol{\xi} \in \Xi$ if a real symmetric matrix $X > 0$ exists such that the generalized Lyapunov inequality*

$$l_{ij}X + m_{ij}(A(\boldsymbol{\xi})\,X + B(\boldsymbol{\xi})\,W) + m_{ji}(X\,A(\boldsymbol{\xi})^T + W^T\,B(\boldsymbol{\xi})^T) < 0; \qquad i, j = 1, ..., n \tag{29}$$

*is satisfied.*

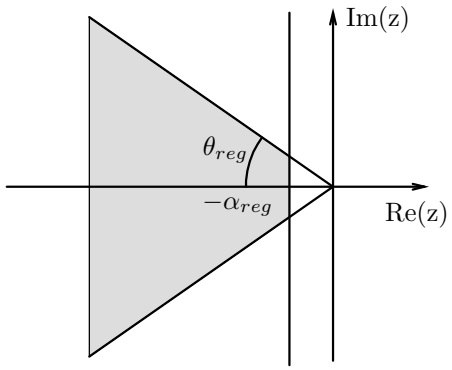


**Figure 5. A typical closed-loop generalized stability region**

In the present design case, the closed-loop eigenvalues are required to lie in the region depicted in Figure 5. Simple computations show that in this case (29) degenerates into

$$\begin{bmatrix} \sin(\theta_{reg})(\Delta(\boldsymbol{\xi}) + \Delta(\boldsymbol{\xi})^T) & \cos(\theta_{reg})(\Delta(\boldsymbol{\xi})^T - \Delta(\boldsymbol{\xi})) & 0 \\ \cos(\theta_{reg})(\Delta(\boldsymbol{\xi}) - \Delta(\boldsymbol{\xi})^T) & \sin(\theta_{reg})(\Delta(\boldsymbol{\xi}) + \Delta(\boldsymbol{\xi})^T) & 0 \\ 0 & 0 & \Delta(\boldsymbol{\xi}) + \Delta(\boldsymbol{\xi})^T + 2\alpha_{reg} X \end{bmatrix} < 0, \tag{30}$$

where $\Delta(\boldsymbol{\xi}) = A(\boldsymbol{\xi})\, X + B(\boldsymbol{\xi})\, W$ and parameters $\alpha_{reg}$ and $\theta_{reg}$ were set to $\alpha_{cl} = 0.1$, and $\theta_{cl} = 45^o$, respectively, so as to meet the desired closed-loop performance specifications.

The optimal solution for the continuous-time $H_2$ control problem is approximated through the minimization of $\zeta$ subject to the LMIs presented in (26) and (30).

### C. Computation of the LPV System Matrices

To define a polytopic LPV model, we consider the parameter vector $\boldsymbol{\xi} = (V_r, \gamma, \theta_{_B}, \delta_f)$ and partition the parameter domain into the convex regions, which result from the combination of intervals defined for each of the parameters. The values for these intervals that were selected to encompass a wide range of operating conditions, are presented in Tables 1 and 2 for the glideslope and flare maneuvers, respectively. For the glideslope maneuver, the reader should notice that due to the design constraint on the common mode of the ailerons at trimming $\delta_{a_C} = 0$, the aircraft pitch angle is not an explicit schedule parameter due to the fact that given a flight path angle $\gamma$ and the constraint $\delta_{a_C} = 0$ the resulting value for the pitch angle at trimming is automatically determined. We also impose null roll and yaw angles ($\phi_{_B} = 0$, $\psi_{_B} = 0$). Further notice that there is overlapping between adjacent parameter regions, which is used to implement an hysteresis switch between controllers.

| Parameter | Interval |
|---|---|
| V | [17.9, 21.1], [20.9, 23.1] m/s |
| $\gamma$ | [-0.07, 0.03] rad |
| $\delta_f$ | [0, 0.16], [0.14, 0.26], [0.24, 0.31] rad |

**Table 1. Glideslope regions intervals ($\delta_{a_C} = 0$)**

| Parameter | Intervals |
|---|---|
| V | [16.9, 18.6], [18.4, 20.1] m/s |
| $\gamma$ | [-0.025, 0.125] rad |
| $\theta_{_B}$ | [0, 0.055], [0.045, 0.105] rad |

**Table 2. Flare regions intervals ($\delta_f = 0.3$ rad)**

Within each region, the state space matrices of the continuous-time system (20) were approximated by an affine function of $\boldsymbol{\xi}$ using Least Squares Fitting applied to a relatively dense grid of evaluated operating points. Then, the resulting system was evaluated at the vertices of each region, producing the finite set of state space matrices needed for control system design.

To access the validity of this approach, we present a simple comparison between the nonlinear model and the LPV-based model. Suppose the aircraft verifies a trimming condition and that the ailerons differential mode suffers a stepwise transition, at given time instant, with a small amplitude. Hence, the main affected states will be the Euler angles of the vehicle. Figure 6 shows the time evolution of the Euler angles for both models, when the aircraft speed is 21.1 m/s and the corresponding path is a straight line.

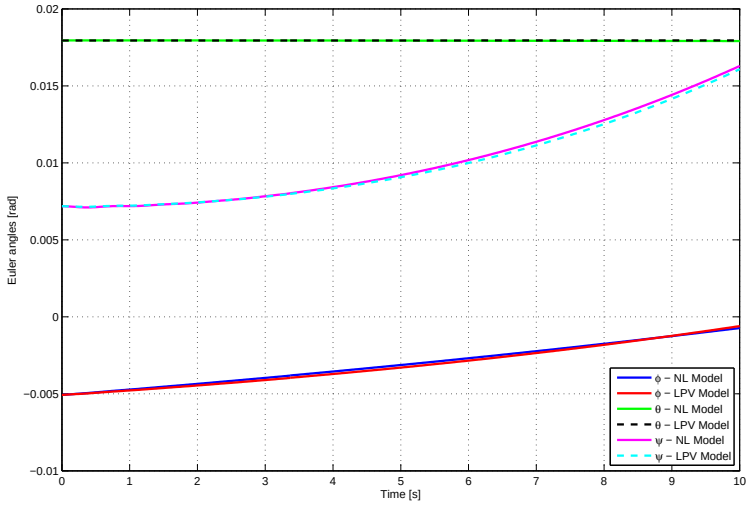


**Figure 6. Comparison between the nonlinear and the LPV-based models**

## D. Augmented Synthesis Model

Consider the system shown in Figure 7, where $P_e$ is the augmented linearized model of the aircraft error dynamics, and $K$ is the state feedback controller to be designed. Block $G$ is the synthesis model that serves as an interface between the designer and the controller synthesis algorithm. This model is obtained by appending the weights $W_1$, $W_2$ and $W_3$ to the linearized error dynamics defined in Section III. These weights serve as tuning "knobs" which the designer can adjust to meet the desired performance specifications.

In the figure, $\mathbf{w}_1$ represents the error space disturbance signals to be rejected. Vector $\mathbf{w}_2$ includes the input noise to each sensor and also accounts for disturbance inputs to the plant states. The signal $\mathbf{u}$ represents the system control inputs, and vector $\mathbf{x}_e + \mathbf{w}_1$ is the state error vector with the added disturbances and sensor noise. Matrices $W_i$, $i = 1, \ldots, 3$ correspond to dynamic weights that penalize input, state, and error variables, while $\mathbf{z} = [\mathbf{z}_1 \quad \mathbf{z}_2 \quad \mathbf{z}_3]^T$ is the performance output vector.

To guarantee that the control loop bandwidth for the deflection surfaces channels and thrust does not exceed 5 rad/s, thereby ensuring that the actuators are not driven beyond their normal actuation bandwidth, the matrix operator $W_2$ was set to

$$W_2(s) = 50\frac{s+5}{s+50}I_{5\times5}$$

where $I_{5\times5}$ denotes the $5 \times 5$ identity matrix. The inclusion of these high-pass weights expedites the process of fine tuning the closed-loop bandwidths of the control planes by penalizing high frequency components of the actuation signals. Operators $W_1$ and $W_3$ were set to constant diagonal matrices.

## E. Nonlinear Controller implementation

The final implementation scheme, presented in Figure 8, results from applying the D-methodology described in Ref. 17. This methodology moves all integrators to the plant input, and adds differentiators where they

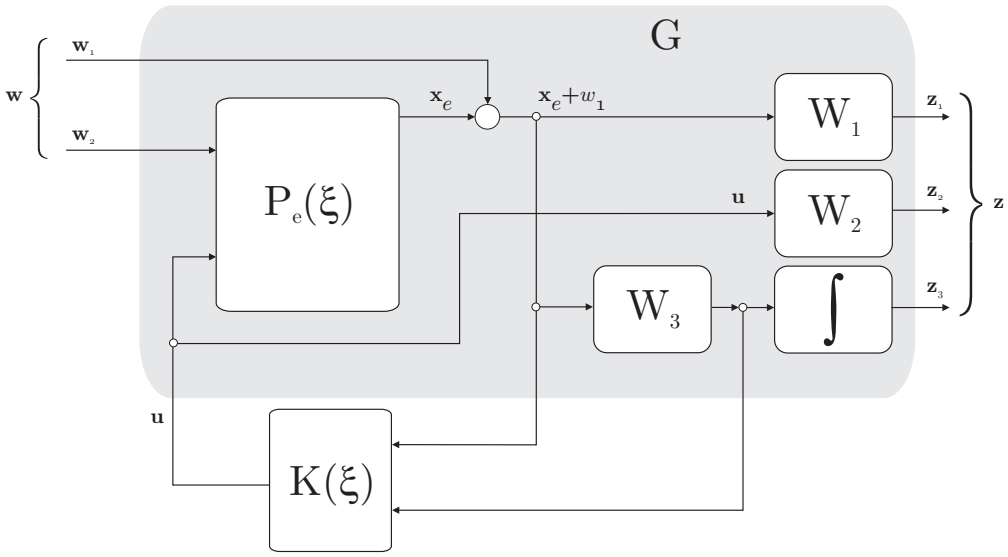


**Figure 7. Augmented synthesis model**

are needed to preserve the transfer functions and the stability characteristics of the closed-loop system. The D-methodology implementation has several important features that are worthwhile emphasizing: i) auto-trimming property - the controller automatically generates adequate trimming values for the actuation signals and for the state variables that are not required to track reference inputs; ii) the implementation of anti-windup schemes is straightforward, due to the placement of the integrators at the plant input. In the figure vectors $\mathbf{x}_e$ and $\mathbf{x}_D$ represent

$$\mathbf{x}_e = \left[\mathbf{v}_e,\ \boldsymbol{\omega}_e,\ \mathbf{d}_t,\ \boldsymbol{\lambda}_e,\ x_1,\ \mathbf{x}_2,\ x_3\, or\, x_4\right]^T \qquad \text{and} \qquad \mathbf{x}_D = \begin{bmatrix} \phi_e \\ \left(\mathbf{v}_e + {}^B_T\mathbf{R}\,[0\ \mathbf{d}_T^T]^T\right) \end{bmatrix}^T, \tag{31}$$

respectively. Notice the switch that selects the angle $\theta_e$ while in the flare maneuver and $\delta_{aC}$ while in the glideslope.

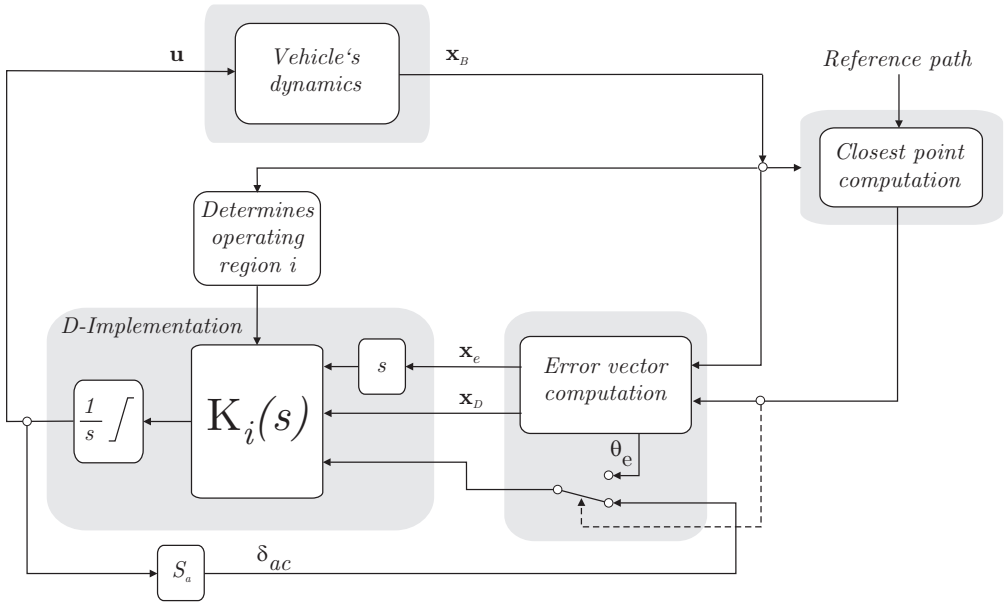


**Figure 8. Gain scheduling and D-methodology**

## F. Landing Maneuvers

Next, the maneuvers for both landing phases are presented. We assume the runway approaching maneuver has been completed which means that the aircraft is already aligned with the runway, at a predefined height, and ready for the glideslope to start.

### 1. *Glideslope Maneuver*

During the glideslope, the aircraft should have a constant flight path angle, $\gamma_{gs}$, corresponding to a straight-line descending path until the start of the flare maneuver. Also, the airspeed should decrease along the path and the roll angle should be close to zero. It should be noticed that the aircraft AOA is not imposed. In fact, as the common mode of the ailerons is automatically driven to zero, the AOA will depend on the airspeed, on the flaps deflection, and on the load of the aircraft.

### 2. *Flare Maneuver*

The flare maneuver starts when the aircraft is at a predefined height. Then, the vehicle should describe a path parameterized by

$$\begin{aligned} z_r(x(t)) &= -k_z e^{-(x(t)-x_f)/\mu} \\ y_r(t) &= y_r \end{aligned} \tag{32}$$

where $\mu = \frac{z_{gs}}{k_z \tan \gamma_{gs}}$ and $x_f = k_z \mu \log(-z_{gs}/k_z) + x_{gs}$. The constant $k_z = 1$ m is a normalizing factor, $x_{gs}$, $y_{gs}$ and $z_{gs}$ are the $x$, $y$ and $z$ coordinates, respectively, of the aircraft's CM at the end of the glideslope. These expressions guarantee not only the continuity of the path when the transition from the glideslope to the flare occurs, but also of its gradient, so that no discontinuities on the reference velocity of the airplane are induced. The resulting reference velocity, $\mathbf{v}_{ref}$, is tangent to that path and is given by

$$\mathbf{v}_{ref} = u_r(t) \begin{bmatrix} 1 \\ 0 \\ k_z e^{-(x(t)-x_f)/\mu} \end{bmatrix}. \tag{33}$$

Finally, the roll and yaw angles should be zero and the reference for the pitch angle $\theta_C$ should be set to the pitch angle required for the vehicle at touchdown. This specific value depends on the airplane's characteristics and load. Figure 9 illustrates the flare reference path. Notice that the $x : y$ aspect ratio was intentionally modified for the sake of clarity.

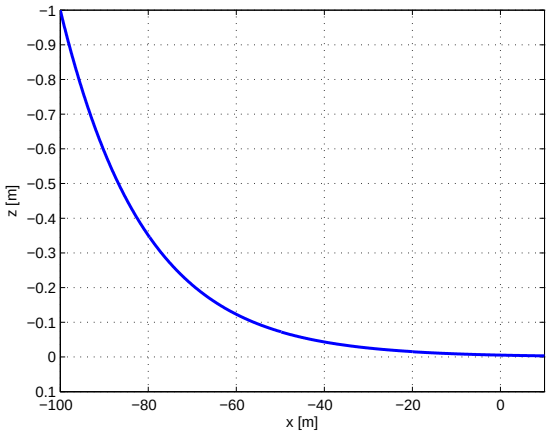


**Figure 9. Flare path for $[x_{gs} \quad y_{gs} \quad z_{gs}]^T = [-100 \quad 0 \quad -1]^T$ m and $\gamma_{gs} = 3$ deg**

## V. Simulation Results

To assess the performance of the proposed autolanding guidance and control law, this section presents a series of simulation results that illustrate the behavior of the nonlinear closed-loop system subject to wind disturbances that simulate different weather conditions during the landing phase. Figure 10 depicts the different stages of a typical landing maneuver, illustrating the evolution of the flaps deflection angle as function of the aircraft height. In the present case, the aircraft should land on a $x$ aligned runway with desired touchdown point located at the origin of the inertial reference frame. For each of the four examples

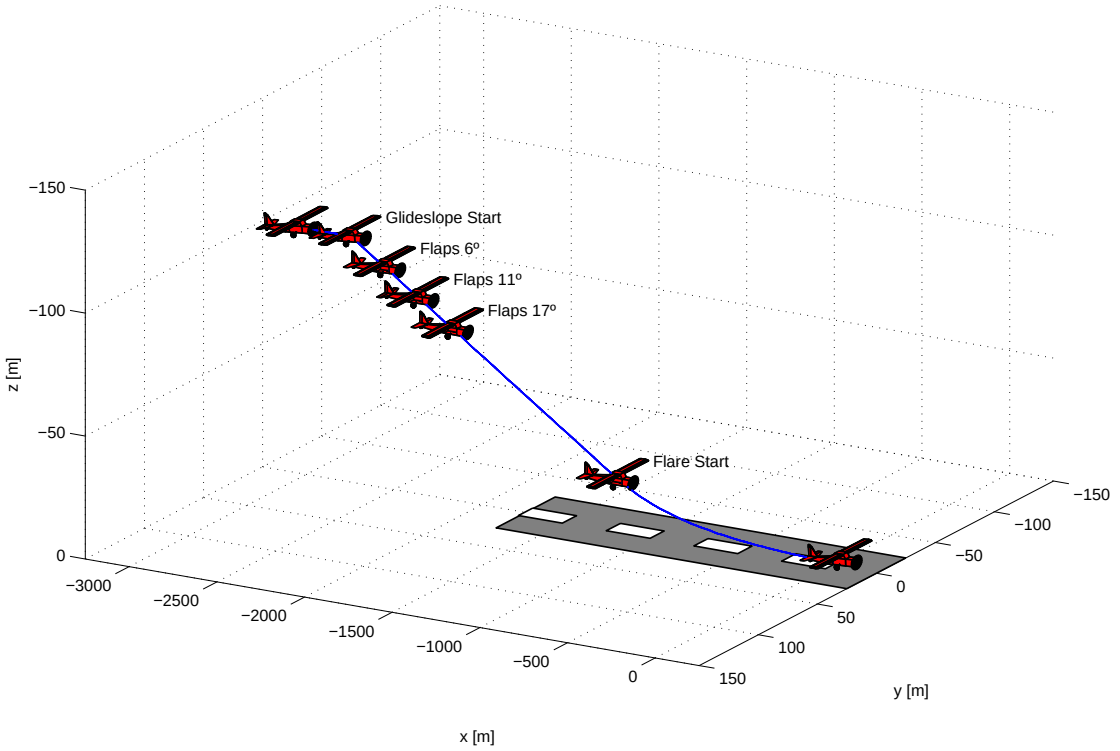


**Figure 10. A typical landing maneuver**

presented hereafter, the results were obtained after five Monte-Carlo runs. It should be noticed that, since our model-airplane only weights about 20 kg, the wind disturbances affect largely the performance of the closed-loop system, limiting the attainable operational flight envelope under severe weather conditions. In the simulations, the mean value of the wind disturbance vector was set to $\bar{\mathbf{v}}_W = [\bar{u}_{wind}, 0, 0]^T$, which corresponds to front wind aligned with the runway. The stochastic component of the wind disturbances was generated according to the Dryden spectrum, see Ref. 19 for details.

### A. Case A1

Figure 11(b) illustrates the time evolution of the aircraft linear velocity. From the figure, one can conclude that the component $v$ of the body velocity is small, resulting in an adequately negligible sideslip angle during the entire maneuver. The $w$ component of the body velocity is positive as desired while landing to increase the lift for a given airspeed. Notice also that the speed of the aircraft decreases as it approaches touchdown.

Figure 12(a) shows the time evolution of the $y$ and $z$ components of the aircraft linear position. The different phases of the landing maneuver are depicted, and the unlabeled initial stage corresponds to a runway aligning maneuver that naturally precedes the glideslope. Figure 12(b) illustrates the time evolution of the aircraft's Euler angles. Notice the tracking characteristics of the pitch angle during the flare which should be close to 3 deg at touchdown.

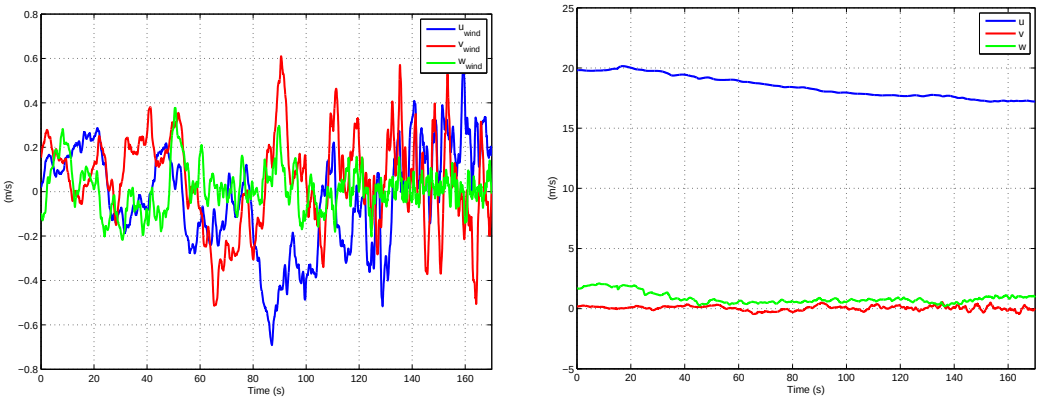


(a) Dryden spectrum wind disturbances

(b) Rigid body linear velocities

**Figure 11. Case A1 wind disturbances and rigid body velocities**

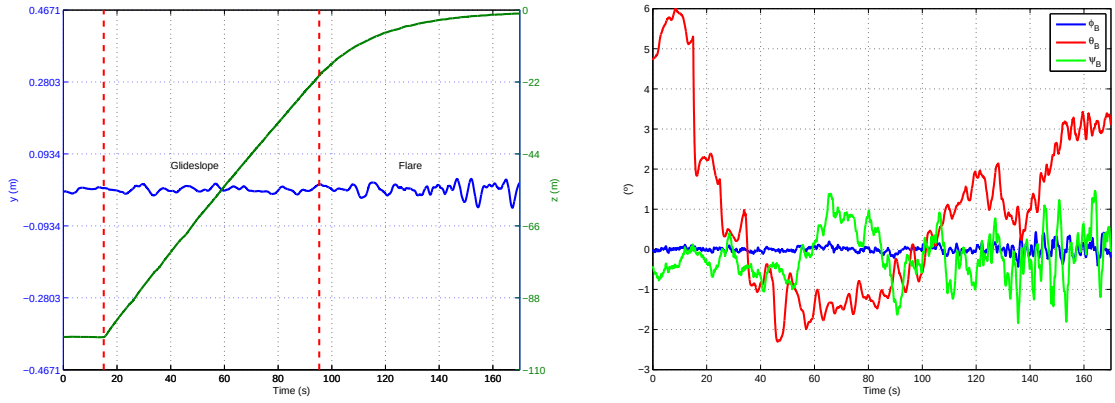


(a) Vehicle's $y$ and $z$ position coordinates on inertial frame

(b) Vehicle's Euler angles

**Figure 12. Case A1 vehicle's $y$ and $z$ position coordinates and Euler angles**

Finally, Figure 13 presents the actuation signals. We emphasize the effect of using a washout on the common mode of the ailerons during the glideslope maneuver which forces the steady state value of this actuation signal to zero. Due to the use of dynamic weights during the controller design phase, the high-frequency components are significantly reduced. Note that the deflection surface are working far from saturation, which happens at 30 degrees.

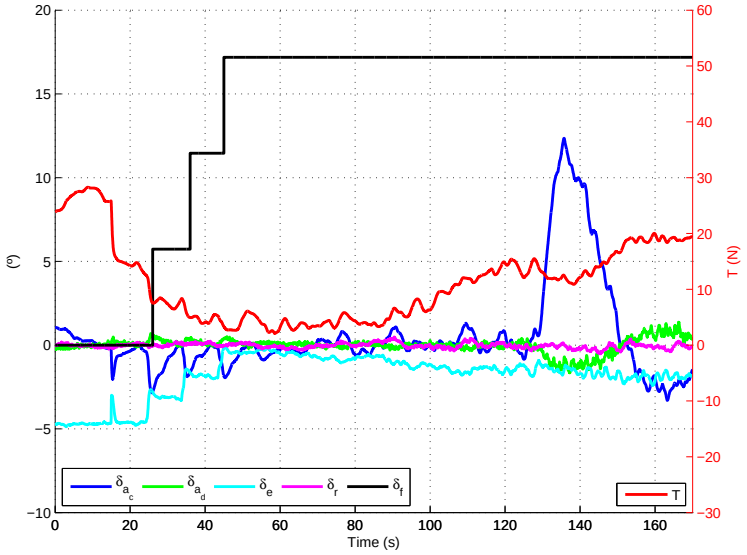


**Figure 13. Airplane's actuation for case A1**

Table 3 shows the RMS values of the most important variables. Notice that the wind disturbances and the RMS value of the body lateral velocity have the same order of magnitude. Since the RMS values of the linear position $y$ and the yaw angle $\psi_B$ are small, we can conclude that a good alignment with the runway is attained.

| | $u_{wind}$ | $v_{wind}$ | $w_{wind}$ | $v_{body}$ | $y$ | $\delta_{a_d}$ | $\delta_r$ | $\phi_B$ | $\psi_B$ |
|---|---|---|---|---|---|---|---|---|---|
| RMS | 0.2351 | 0.2082 | 0.0100 | 0.1841 | 0.0106 | 0.4446 | 0.1498 | 0.10479 | 0.59457 |

**Table 3. RMS values of variables for Case A1. Units are: angles - degrees, positions - m, velocities - m/s.**

**Case A2** To evaluate the impact of the magnitude of the disturbances on the RMS value of the output variables, the full nonlinear system was evaluated under different conditions yielding the results displayed in Table 4.

| | $u_{wind}$ | $v_{wind}$ | $w_{wind}$ | $v_{body}$ | $y$ | $\delta_{a_d}$ | $\delta_r$ | $\phi_B$ | $\psi_B$ |
|---|---|---|---|---|---|---|---|---|---|
| RMS | 0.0783 | 0.0696 | 0.0333 | 0.0620 | 0.0039 | 0.3448 | 0.0620 | 0.0415 | 0.1997 |

**Table 4. RMS values of variables for Case A2. Units are: angles - degrees, positions - m, velocities - m/s.**

## B. Case B

Next, we consider a more challenging situation: a wind gust is experienced during the landing maneuver. The wind disturbances are depicted in Figure 14(a). As in the previous case, the Dryden spectrum was used to generate the wind disturbances and, at a given time, a downward wind gust, with magnitude of 5 m/s and the duration of 2 s, is added. The effect of the turbulence on the vehicle's linear velocities is shown in Figure 14(b).

Figures 15(a) and 15(b) show how the wind gust affects the vehicle's $y$ and $z$ coordinates and Euler angles, respectively. Notice that the magnitude of the wind gust is over 25% of the aircraft airspeed. Due

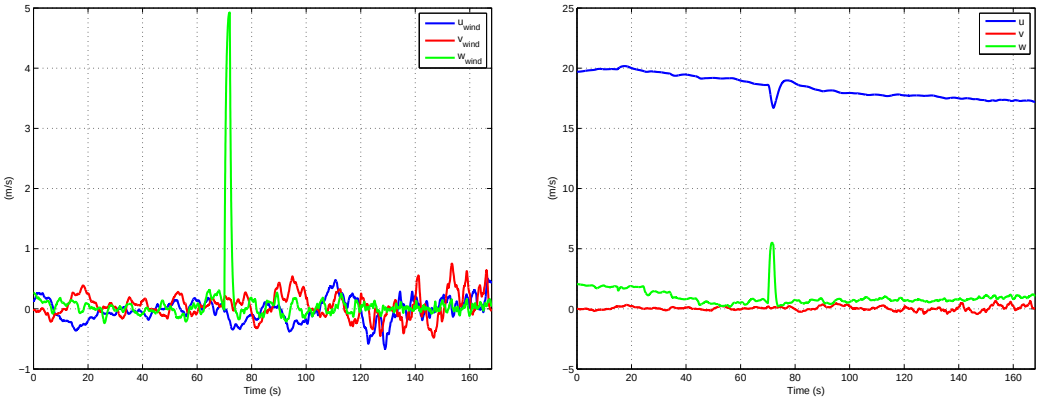


(a) Dryden spectrum wind disturbances

(b) Rigid body linear velocities

**Figure 14. Case B wind disturbances and rigid body velocities**

to the rate and amplitude limitations of the actuators and the low airspeed, the aircraft cannot completely compensate for the effect of the disturbances. Nonetheless, it takes only about 5 s for the aircraft to recover from the disturbance.

As shown in Figure 15(b) the aircraft pitch angle tends to increase in the presence of a downwards wind gust. This is due to the fact that the airplane is longitudinally stable, which means the neutral point is aft the center of mass. Thus, a downwards wind disturbance generates a nose up moment, which increases the AOA and therefore the lift force, hence compensating for the disturbance.

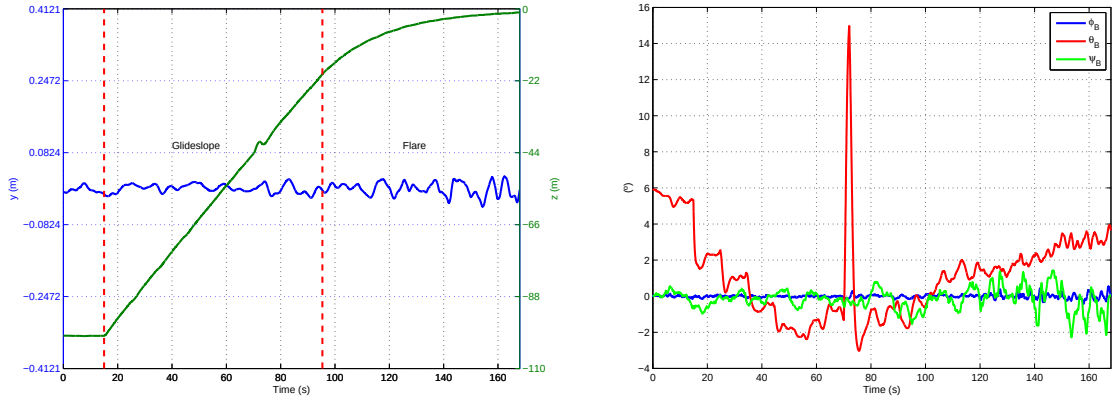


(a) Vehicle's $y$ and $z$ position coordinates on inertial frame

(b) Vehicle's Euler angles

**Figure 15. Case B vehicle's $y$ and $z$ position coordinates and Euler angles**

Figure 16 presents the aircraft's actuation signals. From the figure, it can be seen that the fast response of the controller allows a short recovery time of about 5 s.

## C. Case C

Finally, we consider a worst case situation simulating an upward wind gust immediately followed by a downwards wind gust (see Figure 17(a)). This can be a very hard disturbance rejection problem as the rate limitation of the actuators together with the low aircraft airspeed give rise to a trade off between recovery time and the capability of dealing with sudden changes on the wind direction.

Figures 17(b), 18(a) and 18(b) display the behavior of the aircraft for case C, whose interpretation is similar to that of case B. As in previous cases the control signals for the actuators are smooth, (see Figure 19). Moreover, the recovery time does not go beyond 10 s under these severe disturbances.

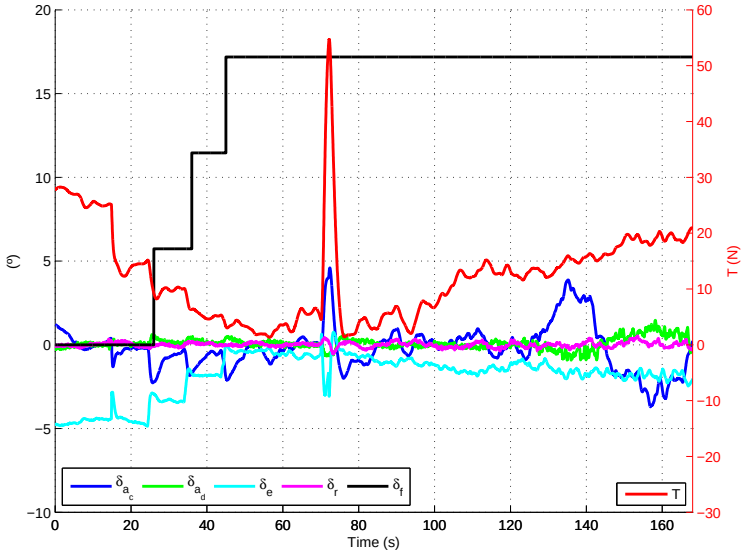


**Figure 16. Airplane's actuation for case B**

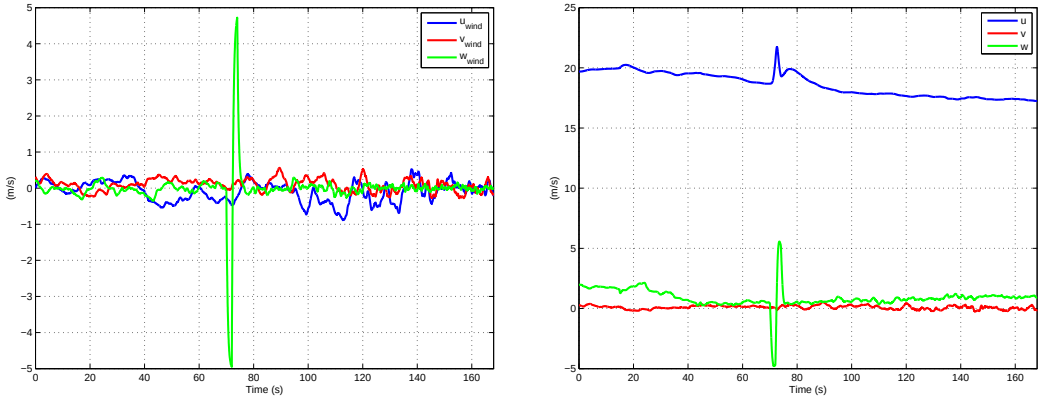


(a) Dryden spectrum wind disturbances

(b) Rigid body linear velocities

**Figure 17. Case C wind disturbances and rigid body velocities**

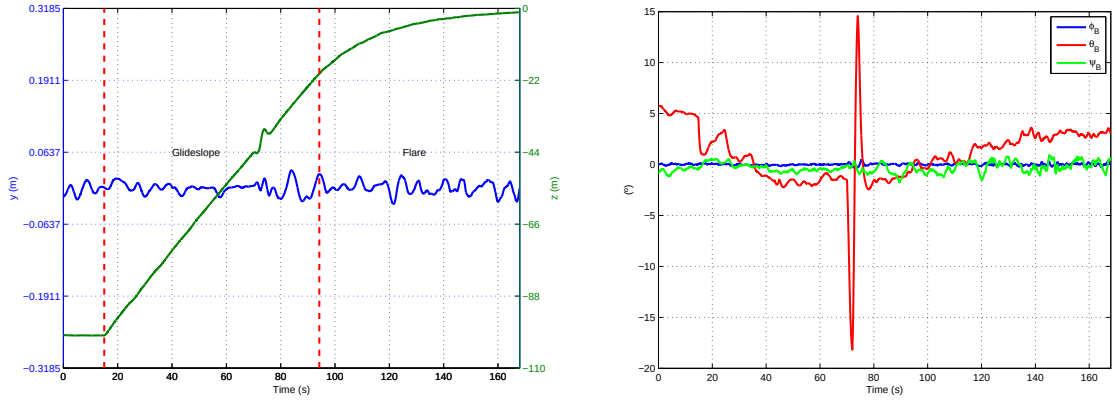


(a) Vehicle's $y$ and $z$ position coordinates on inertial frame

(b) Vehicle's Euler angles

**Figure 18. Case C vehicle's $y$ and $z$ position coordinates and Euler angles**

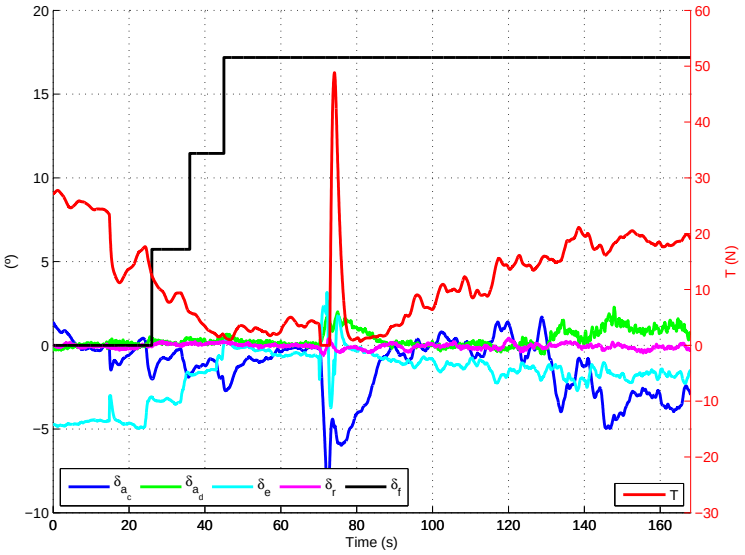


**Figure 19. Airplane's actuation for case C**

## VI. Conclusions

The paper presented a solution to the autolanding guidance and control problem for an unmanned autonomous vehicle (UAV) based on the information provided by the onboard Navigation System. The proposed solution relies on a path-following and velocity profile tracking controller synthesized using an accurate aircraft dynamic model, referred to as *SymAirDyn*, that was designed with the objective of exploiting the whole aircraft's flight envelope. An $H_2$ controller design methodology for polytopic LPV systems was adopted, taking advantage of dynamic weights to limit the actuation bandwidth. The technique presented relies on a new error space that naturally describes the particular dynamic characteristics of the aircraft over a suitable flight envelope. The effectiveness of the new control law was assessed in a simulation environment with the full nonlinear aircraft model, *SymAirDyn*, under different types of disturbances that affect severely the aircraft's behaviour. The quality of the results obtained clearly indicates that the methodology derived is suitable for the proposed application.

## Acknowledgments

This work was partially supported by Fundação para a Ciência e a Tecnologia (ISR/IST pluriannual funding) through the POS_Conhecimento Program that includes FEDER funds.

## References

[1]Shakernia, O., Vidal, R., Sharpy, C. S., Ma, Y., and Sastry, S., "Multiple View Motion Estimation and Control for Landing an Unmanned Aerial Vehicle," *ICAR*, USA.

[2]Johnson, E. N. and Schrage, D. P., "The Georgia Tech Unmanned Aerial Research Vehicle: GTMax," *AIAA Guidance, Navigation and Control Conference*, Austin, TX.

[3]Wills, L., Kannan, S., Sander, S., Guler, M., Heck, B., Prasad, J. V. R., Schrage, D., and Vachtsevanos, G., "An openplatform for reconfigurable control," *Control Systems Magazine, IEEE*, Vol. 21(3), 2001, pp. 49–64.

[4]*ICAO Annex 10 Volume 1, Radio Navigation Aids, Fifth Edition – July 1996*.

[5]Vasconcelos, J. F., Silvestre, C., and Oliveira, P., "Embedded Vehicle Dynamics and LASER Aiding Techniques for Inertial Navigation Systems," *AIAA Guidance Navigation and Control Conference*, Keystone, CO, USA.

[6]Kaminer, I., Pascoal, A., Hallberg, E., and Silvestre, C., "Trajectory Tracking for Autonomous Vehicles: An Integrated Approach to Guidance and Control," *AIAA Journal of Guidance, Control, and Dynamics*, Vol. 21, No. 1, 1998, pp. 29–38.

[7]Silvestre, C., Pascoal, A., and Kaminer, I., "On the Design of Gain-Scheduled Trajectory Tracking Controllers," *International Journal of Robust and Nonlinear Control*, Vol. 12, 2002, pp. 797–839.

[8]Cabecinhas, D., Silvestre, C., Rosa, P., and Cunha, R., "Path Following Control for Coordinated Turn Aircraft Maneuvers," *AIAA Guidance and Control Conference (Submitted)*, 2007.

[9]Cunha, R., Antunes, D., Gomes, P., and Silvestre, C., "A Path-Following Preview Controller for Autonomous Air Vehicles," 2006.

[10]Lim, J., Song, J., and Sung, K. M., "Forward-Backward Time Varying Forgetting Factor Kalman Filter based DOA Estimation Algorithm for UAV Autolanding," Tech. rep., Seoul National University, 2002.

[11]Juang, J.-G., Chang, H.-H., and Cheng, K.-C., "Intelligent Landing Control Using Linearized Inverse Aircraft Model," *Proceedings of the American Control Conference - Anchorage, AK*, 2002.

[12]Shue, S.-P. and Agarwal, R. K., "Design of Automatic Landing Systems Using Mixed $H_2/H_\infty$ Control," *Journal of Guidance, Control and Dynamics*, Vol. 22(1), 1999, pp. 103–114.

[13]Frazzoli, E., Dahleh, M., and Feron, E., *A Hybrid Control Architecture for Aggressive Maneuvering of Autonomous Aerial Vehicles*, In Advances in Systems Theory, Kluwer Academic Publishers, 1999.

[14]Civita, M. L., Papageorgiou, G., Messner, W. C., and Kanade, T., "Design and Flight Testing of a High-Bandwidth $H_\infty$ Loop Shaping Controller for a Robotic Helicopter," *AIAA Guidance, Navigation and Control Conference*, Monterey, CA.

[15]Rugh, W. J. and Shamma, J. S., "Research on gain scheduling," *Automatica*, Vol. 36, 2000, pp. 1401–1425.

[16]Marcos, A. and Balas, G. J., "Development of Linear-Parameter-Varying Models for Aircraft," *AIAA Journal of Guidance, Control and Dynamics*, Vol. 27(2), 2004, pp. 218–228.

[17]Kaminer, I., Pascoal, A., Khargonekar, P., and Coleman, E., "A Velocity Algorithm for the Implementation of Gain-Scheduled Controllers," *Automatica*, Vol. 31, No. 8, 1995, pp. 1185–1191.

[18]Schmidt, L. V., *Introduction to Aircraft Flight Dynamics*, AIAA Education Series, 1998.

[19]Stengel, R. F., *Flight Dynamics*, Princeton University Press, Flight Dynamics.

[20]Lyashevskiy, S. and Chen, Y., "Nonlinear Identification of Aircraft," *Proceedings of the 1996 IEEE lnternational Conference on Control Applications*, 1996.

[21]Brederode, V., *Fundamentos de Aerodinmica Incompressvel*, Author's publication, Department of Mechanical Engineering, Instituto Superior Tecnico, Lisboa, Portugal, 1997.

[22]Craig, J. J., *Introduction to Robotics and Control: Mechanics and Control, 2nd ed.*, Addison-Wesley Publishing Company, Massachusetts, 1989.

[23]Cunha, R., Antunes, D., and P. Gomes, C. S., "A Path-Following Preview Controller for Autonomous Air Vehicles," *AIAA Guidance Navigation and Control Conference, Keystone, CO, USA*, 2006.

[24]Cunha, R. and Silvestre, C., "A 3D Path-Following Velocity-Tracking Controller for Autonomous Vehicles," *16th IFAC World Congress*, Praha, Czech Republic, July 2005.

[25]Ghaoui, L. E. and Niculescu, S. I., editors, *Advances in Linear Matrix Inequality Methods in Control*, Society for Industrial and Applied Mathematics, SIAM, Philadelphia, PA, 1999.

[26]Boyd, S., Ghaoui, L. E., Feron, E., and Balakrishnan, V., *Linear Matrix Inequalities in Systems and Control Theory*, Society for Industrial and Applied Mathematics, SIAM, Philadelphia, PA, 1994.

[27]Ghaoui, L. E. and Niculescu, S. I., editors, *Advances in Linear Matrix Inequality Methods in Control*, Society for Industrial and Applied Mathematics, SIAM, Philadelphia, PA, 1999.

[28]Scherer, C. and Weiland, S., *Lecture Notes on Linear Matrix Inequalities in Control*, Dutch Institute of Systems and Control, 2000.

[29]Chilali, M. and Gahinet, P., "$H_\infty$ design with pole placement constraints: an LMI approach," *IEEE Transactions*, Vol. AC-41, No. 3, mar 1996, pp. 358–367.